

Enhanced photocatalytic reduction of carbon dioxide in optical fiber monolith reactor with transparent glass balls

Huiyao Chen¹, Fengming Chu¹, Lijun Yang^{1*}, Oluwafunmilola Ola^{2*}, Xiaoze Du¹, Yongping

Yang¹

1. Key Laboratory of Condition Monitoring and Control for Power Plant Equipment of Ministry of Education

School of Energy Power and Mechanical Engineering, North China Electric Power University, Beijing 102206, China

2. College of Engineering, Mathematics and Physical Sciences, University of Exeter, Exeter, EX4 4QF, United Kingdom

Abstract

Photocatalytic reduction of carbon dioxide to produce methanol is a promising approach to restrain greenhouse gases emissions and mitigate energy shortage, which attracts extensive concerns in recent years. The optical fiber monolith reactor with solid glass balls for photocatalytic carbon dioxide reduction is proposed in this work to increase the product concentration, and the glass balls are transparent and coated with photocatalysts evenly to absorb light. The photocatalytic reduction of carbon dioxide in optical fiber monolith reactor is numerically investigated, by which the effects of glass ball number, location, circle and layer on the production are analyzed. The results show that in the single-circle and single-layer model, the outlet methanol concentration

* Corresponding author: Lijun Yang. Tel: +86(10)61773373; Fax: +86(10)61773877.
Email address: yanglj@ncepu.edu.cn
Oluwafunmilola Ola. Tel: +44 (0) 139 272 5492. E-mail address: O.Ola@exeter.ac.uk

increases with increasing the ball number. The closer to the fiber and reactor inlet the balls keep, the higher the methanol production is. As the circle and layer numbers increase, the methanol concentration also increases. The outlet methanol average concentration of the optical fiber monolith reactor with 3-circle and 5-layer balls gets 11.43% higher than the case without glass balls.

Key words: Photocatalytic; Carbon dioxide reduction; Methanol production; Optical fiber monolith reactor; Glass balls

Nomenclature

C	concentration, mol m ⁻³
d	diameter, m
D	diffusion coefficient, m ² s ⁻¹
f_{θ}	fraction of incident light with incident angle less than 90°
I	light intensity, W m ⁻²
k	kinetic rate constant, m ⁴ s ⁻¹ mol ⁻²
K	adsorption equilibrium constant
l	distance, mm
L	reactor length, mm
M	relative molecular mass
n	number
p	pressure, Pa
P	total pressure, Pa
r	reaction rate, mol m ⁻³ s ⁻¹
R	radius, mm
T	temperature, K
u	velocity, m s ⁻¹
V	molar volume, cm ³ mol ⁻¹
z	axial position, mm
Greek letters	
α	refractive loss coefficient, cm ⁻¹

β	attenuation coefficient of the tip light flux, cm^{-1}
δ	catalyst film thickness, nm
ε	local attenuation coefficient of catalyst thin-film, cm^{-1}
η	energy conversion efficiency
μ	molecular weight of gas
ν	viscosity, $\text{m}^2 \text{s}^{-1}$
ρ	density, kg m^{-3}
θ	circumferential coordinate, rad
σ	fractional surface coverage
λ	overall factor
ϕ	quantum efficiency

Subscript and superscript

f	optical fiber
fc	fiber coating
l	layer
m	monolith
mc	monolith coating
gs	glass ball
gsc	glass ball coating
w	monolith channel wall
r	radius direction in cylindrical coordinate system
θ	circumferential direction in cylindrical coordinate system

z

axial direction in cylindrical coordinate system

1. Introduction

The continuous development of world economy and progress of human civilization since the industrial revolution of mankind basically depend on the adequate energy supply, generally fossil fuels [1]. However, the non-renewable characteristics of fossil fuels compel human explore the renewable sources aiming at sustainable development [2]. Besides, the carbon flow between the ocean and the atmosphere should be natural while human activity adds too much CO₂ to that cycle [3]. Typically, the burning of fossil fuels produces a large amount of greenhouse gases, mainly carbon dioxide [4], resulting in many environmental issues such as global warming [5]. Therefore, the great challenge for the mankind is to take powerful measures to develop alternative renewable energy resources [6] and reduce atmospheric CO₂ concentrations [7]. Among various CO₂ capture technologies [8], it seems practical and alternative to take advantage of the MEA (monoethanolamine) and ammonia aqueous solution absorption in packed absorbing columns [9, 10] or bubble columns [11], hydrate-based biogas upgrading with CO₂ valorization [12] and artificial photosynthesis in photoreactors [13], etc. Besides, using coal fly ash is an available and potential way to store carbon dioxide [14], and the conversion to fuels as well as the utilization of CO₂ also attracts extensive attention [15]. It is potential that methanol synthesis using captured CO₂ could reduce CO₂ emission and produce the clean fuel [16]. With the efforts of many scholars, the technologies of photocatalytic reduction of CO₂ have made great progress [17], among which the CO₂ photo-hydrogenation by mimicking photosynthesis is one of the best routes of obtaining renewable hydrocarbon fuels under

the sunlight and action of photocatalyst in photoreactors [3]. This method is effective to reduce the atmospheric CO₂ concentration and relieve global energy shortage [18]. However, the hydrocarbon yield is commonly low [19] due to the limited reaction surface area, so many researchers aim at improving the photoreactor structure to promote the CO₂ reduction [20] and hydrocarbon conversion [21].

In previous studies, various photoreactors such as slurry reactor, fixed bed reactor, surface coated reactor, twin reactor [22], optical fiber photocatalytic reactor [23], annular and bubble flow reactors [24] were proposed, for which the structures play an important role in the CO₂ photoreaction. For optical fiber monolith reactor (OFMR), the optical fiber is inserted into the parallel reaction channels, and the catalyst is coated on the fiber and monolith surfaces to convert the CO₂ to methanol under the artificial light [25, 26]. This type of photoreactor shows many advantages over other photoreactors [27], such as the efficient and uniform light distribution, good interaction between the catalyst layer and photons, high conversion efficiency and product yield, low pressure drop and operational costs [28], so it seems more promising for the photocatalytic CO₂ reduction [29].

For the OFMR, the solar energy utilization ratio for the CO₂ photoreduction is only around 3% and the reaction surface area is not large enough, which shows a wide space to increase the solar energy conversion efficiency and improve the photocatalytic CO₂ reduction [20]. In the aforementioned studies, more emphases were placed upon the energy conversion efficiency and modified effective photocatalysts, while the photoreactor structure is still worthy of further investigation [23].

As a credible way of OFMR, a bundle of optical fibers like honeycomb is commonly used to transmit the light with solar concentrating devices and increase the reaction surface area. In this work, a filling transparent solid glass ball model is proposed in the light of OFMR, where the surfaces of the fiber, monolith, and the glass balls are all coated with photocatalysts to adequately absorb photons for the photocatalytic CO₂ reduction and improve the energy conversion efficiency. By this way, the photoreaction surface area is enlarged without destroying the central symmetric structure of the reactor and the disturbance to the flow is minimized as much as possible. The filling ball model is simulated in this paper using the commercial multi-physics software COMSOL. The numerical simulation can not only verify the reliability and accuracy of the experimental results after the experiments, but also predict the feasibility before the experiments. The yield and the average outlet concentration of the product, the CO₂ concentration and velocity distribution, are all obtained and compared with the photoreaction in the traditional OFMR, which can contribute to the optimal design and energy efficient operation of photocatalytic CO₂ reduction in optical fiber monolith reactor.

2. Multi-physics modeling

Due to the identity of each flow-path, only one reactor unit, namely one channel, is taken into account in this work. The comprehensive and rigorous model is developed, which consists of three computational modules of chemistry, transport of dilute species and creeping flow.

2.1. Physical model

The traditional and proposed models are schematically shown in Fig. 1. In the traditional model, the light source is set at the inlet of channel and perpendicular to the entrance section as shown in Fig. 1(a) [28, 30], with the light intensity kept constant in the experiment. Based on previous studies, the reverse arrangement of the light source is more favorable to the photoreaction [20], so the light source is set at the outlet to emit ultraviolet light in the proposed model, as shown in Fig. 1(b). 15 same transparent solid glass balls coated with photocatalyst layers are placed outside the fiber in the flow-path, increasing the photoreaction surface area in the single channel. The fiber made of quartz glass is set in the center of the channel as a light conductor, labeled as 1, and the quartz glass is assumed to be hyaline to ultraviolet light [31]. The monolith is composed of opaque ceramics, labeled as 2 and the glass balls are labeled as 3. The photocatalyst, consisting of TiO_2 containing 1% $\text{NiO}/\text{InTaO}_4(\text{sg})$, is evenly coated on three surfaces [31]. The reactants of CO_2 and H_2O flow into the channel from the inlet and react in the photoreactor, and the products leave out at the outlet.

The location of the balls in the photoreactor is shown in Fig. 2. Based on the structure of the proposed model, the following assumptions are taken to simplify the model without adhibiting large deviation in numerical simulations:

(1) The glass balls are well-distributed outside the fiber in the same plane with z equal to z_{gs} . The angle between two adjacent balls is θ and the distance from each ball center to fiber center is labeled as r_{gs} , as shown in Fig. 2.

(2) The reaction system maintains a constant temperature of 298 K at which the Arrhenius expression is negligible [28].

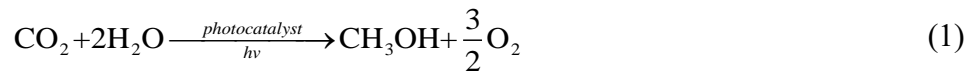
(3) In the channel, all the species are homogeneous, incompressible and isotropic Newtonian fluids.

(4) The flow inside the channel is steady, laminar and fully developed, with no backward flow.

(5) All the transparent glass balls are exactly the same, with the volume and radius of 0.01 mm³ and 0.13365 mm, respectively. The transmissivity of the glass ball is 1, which means the light is only absorbed by the thin-film photocatalyst and the unabsorbed light passes through the glass balls directly without any loss.

(6) Each glass ball is sustained and fixed with a silex glass scaffold on the fiber. The scaffold is extremely fine to avoid disturbing the fluid flows in the channel. Silex glass is transparent to UV light, not preventing the light transmission. Moreover, silex glass is steady and chemically inert, not reacting with various constituents of the fluids. So the scaffolds are ignored in the simulation.

(7) Photocatalytic reaction of carbon dioxide on the photocatalyst film can be described as follows.



It does not focus on the photoreaction mechanism, but the variations of the reactants and products.

2.2. Fluid flow model

For the incompressible viscous fluid flows of CO₂ and H₂O, the Navier-Stokes equation in the columnar coordinate system is adopted with the following form:

$$\frac{\partial u_r}{\partial r} + \frac{1}{r} \frac{\partial u_\theta}{\partial \theta} + \frac{\partial u_z}{\partial z} = 0 \quad (2)$$

$$\begin{aligned}
& u_r \frac{\partial u_r}{\partial r} - \frac{u_\theta^2}{r} + \frac{u_\theta}{r} \frac{\partial u_r}{\partial \theta} + u_z \frac{\partial u_r}{\partial z} \\
&= -\frac{1}{\rho} \frac{\partial p}{\partial r} + \nu \left(\frac{\partial^2 u_r}{\partial r^2} + \frac{1}{r} \frac{\partial u_r}{\partial r} - \frac{u_r}{r^2} - \frac{2}{r^2} \frac{\partial u_\theta}{\partial \theta} + \frac{1}{r^2} \frac{\partial^2 u_r}{\partial \theta^2} + \frac{\partial^2 u_r}{\partial z^2} \right)
\end{aligned} \tag{3}$$

$$\begin{aligned}
& u_r \frac{\partial u_\theta}{\partial r} + \frac{u_r u_\theta}{r} + \frac{u_\theta}{r} \frac{\partial u_\theta}{\partial \theta} + u_z \frac{\partial u_\theta}{\partial z} \\
&= -\frac{1}{\rho r} \frac{\partial p}{\partial \theta} + \nu \left(\frac{\partial^2 u_\theta}{\partial r^2} + \frac{1}{r} \frac{\partial u_\theta}{\partial r} - \frac{u_\theta}{r^2} + \frac{2}{r^2} \frac{\partial u_r}{\partial \theta} + \frac{1}{r^2} \frac{\partial^2 u_\theta}{\partial \theta^2} + \frac{\partial^2 u_\theta}{\partial z^2} \right)
\end{aligned} \tag{4}$$

$$u_r \frac{\partial u_z}{\partial r} + \frac{u_\theta}{r} \frac{\partial u_z}{\partial \theta} + u_z \frac{\partial u_z}{\partial z} = -\frac{1}{\rho} \frac{\partial p}{\partial z} + \nu \left(\frac{\partial^2 u_z}{\partial r^2} + \frac{1}{r} \frac{\partial u_z}{\partial r} + \frac{1}{r^2} \frac{\partial^2 u_z}{\partial \theta^2} + \frac{\partial^2 u_z}{\partial z^2} \right) \tag{5}$$

where u_r , u_θ , u_z are the velocities in the r , θ , z directions. p is the pressure. ρ and ν are the density and viscosity. The corresponding boundary conditions satisfy:

$$u_r = u_\theta = 0, u_z = u_{inlet} \quad z = 0 \tag{6}$$

$$u_r = u_\theta = 0, \frac{\partial u_z}{\partial z} = 0 \quad z = L \tag{7}$$

$$u_r = u_\theta = u_z = 0 \quad \text{Other boundaries} \tag{8}$$

For the reactant gases, marked A and B , the diffusion coefficient D can be obtained from the following semi-empirical formula [32]:

$$D = \frac{435.7T^{3/2}}{P(V_A^{1/3} + V_B^{1/3})^2} \sqrt{\frac{1}{M_A} + \frac{1}{M_B}} \tag{9}$$

Where T is the actual temperature, P is the total pressure and M is the molecular mass of the gas. V is the molar volume with the constant of $22.4 \times 10^3 \text{ cm}^3 \cdot \text{mol}^{-1}$. Comparing with CO_2 , the diffusion coefficients of H_2O , CH_3OH and O_2 can be obtained by Eq. (9).

2.3. Reaction kinetics model

During the photocatalytic CO_2 reduction, the reaction rate is proportional to the absorption of the reactants with different adsorption coefficients, and the product is desorbed from the surface of photocatalyst film. The reaction kinetic equation in the

present work is developed based upon the following two aspects:

(1) Langmuir-Hinshelwood equation is used to fit the photocatalytic reduction rate of CO₂ with the reaction rate expressed as [33]:

$$r = k\sigma_A\sigma_B = k \frac{K_A p_A K_B p_B}{(1 + K_A p_A + K_B p_B)^2} \quad (10)$$

where σ is the surface coverage ratio of reactants; k is the kinetic rate constant; K is adsorption equilibrium constant; p is the partial pressure of each reagent in the mixture.

k and K are both related to the actual temperature.

(2) A power law relation is applied between the total absorbed radiation on photocatalyst films and the kinetic rate constant.

It should be noted that the detachment of the products from photocatalyst film is incomplete, so the reaction active region is covered and the efficiency of photocatalytic reduction of CO₂ is reduced. Furthermore, the reverse reaction may occur to some extent, and part of the resultant methanol is oxidized to CO₂ by oxygen. Therefore, the double effects of photocatalytic reduction and oxidation are both taken into account and the reactants and resultants are supposed to be adsorbed in the same catalyst activity region. Eq. (10) can be modified as the following form [34]:

$$r = kI^n \frac{K_A p_A K_B p_B}{(1 + K_A p_A + K_B p_B + K_C p_C + K_D p_D)^2} \quad (11)$$

where I represents the incident ultraviolet light intensity; n is the power-law coefficient, changing from 0.5 to 1, to describe the reaction rate on account of light intensity. The larger the n value of the photoreactor, the more effective the photocatalyst thin-film sucks up the incident photons [35].

Combining the Eq. (1) and Eq. (11), the kinetic formula follows:

$$r = kI^n \frac{K_{\text{H}_2\text{O}}K_{\text{CO}_2}(p_{\text{H}_2\text{O}}p_{\text{CO}_2})}{(1 + K_{\text{H}_2\text{O}}p_{\text{H}_2\text{O}} + K_{\text{CO}_2}p_{\text{CO}_2} + K_{\text{O}_2}p_{\text{O}_2} + K_{\text{CH}_3\text{OH}}p_{\text{CH}_3\text{OH}})^2} \quad (12)$$

In order to reduce the calculation errors for the photocatalytic CO₂ reduction, three assumptions are made: (a) the dynamic reaction rate and the coverage area of CO₂ are in the direct ratio; (b) the main adsorbent in the photocatalyst film is CO₂ and methanol; (c) the photons arriving at the catalyst coating are entirely taken in, namely the value of n is 1. Therefore, the Eq. (12) is simplified [35]:

$$r = kI \frac{K_{\text{H}_2\text{O}}K_{\text{CO}_2}(p_{\text{H}_2\text{O}}p_{\text{CO}_2})}{(1 + K_{\text{CO}_2}p_{\text{CO}_2} + K_{\text{CH}_3\text{OH}}p_{\text{CH}_3\text{OH}})^2} \quad (13)$$

2.4. Light intensity distribution model

Marinangeli and Ollis [36] put forward a simple exponential decay equation to characterize the distribution of light intensity in an optical fiber coated with a photocatalyst thin-film, as follows:

$$I_{axial}(z) = \exp(-\alpha z)I_{input} \quad (14)$$

where $I_{axial}(z)$ represents the axial light intensity of the optical fiber along the z -axis; I_{input} refers to the light intensity at the entrance of the optical fiber with the z value of 0. α is the refraction loss coefficient gained from the fitting experimental data. However, some other parameters such as the wavelength, refractivity, angle of incidence, catalyst layer thickness, the coating porosity and the length of the fiber also affect the light transfer efficiency (or called diopter) in the photocatalyst thin-film of OFMR [37]. As a result, a new parameter f_θ is introduced to make the equation more reliable [38]:

$$I_{axial}(z) = [(1 - f_\theta) + f_\theta \exp(-\alpha z)]I_{input} \quad (15)$$

f_θ is the percentage of the incident light with the incident angle of less than 90 degrees in total incident light. The fraction $I_{input}(1-f_\theta)$ indicates the light passing through the entire fiber without being absorbed by the photocatalyst film, with the incident direction approximately parallel with the flow channel surface. The greater the f_θ is, the less the ray of light almost parallel to the z -axis is, thereby more difficult to refract from the fiber to the catalyst coating surface. Subsequently, Lin and Valsaraj [26] got success in modeling and measuring the light intensity distribution of every single element in OFMR, based on which the refractive light intensity passing through the photocatalyst film on the fiber decreases by orders of magnitude, but increases clearly at the back of the fiber. Thus, the equation takes the following form:

$$I_f = \frac{1}{4} d_f \left\{ \alpha f_\theta \exp[-(\alpha z + \varepsilon \delta)] I_{input} + \beta \exp[-\beta(L-z)] I_{output} \right\} \quad (16)$$

where β refers to the attenuation coefficient of the top light intensity; ε represents the local attenuation coefficient of the catalyst thin-film, depending on the physical characteristics of the film. β , α , ε and f_θ are all obtained from the experimental data. Besides, I_{output} is the light intensity at the end of the fiber with z equal to L , as follows.

$$I_{output}(L) = [(1-f_\theta) + f_\theta \exp(-\alpha L)] I_{input} \quad (17)$$

So the energy conversion efficiency η can be calculated by the following formula.

$$\eta = f_\theta (1 - \exp(-\alpha L)) \quad (18)$$

In this simulation, it is assumed that the number of photons participating in the photoreaction is constant and the energy conversion efficiency keeps fixed, with the value of 0.294%. The emphases of this research are placed on the improved photoreactor structures to achieve a high product concentration. Besides, in previous

studies, the distribution of ultraviolet transmission light crossing the catalyst coating of the fiber to the honeycomb channel is called Linear Source Spherical Emission, namely LSSE [39]. Hence, the relation between the ultraviolet light intensity and two different coating surfaces satisfies:

$$I_{mc} = \frac{R_f}{R_m} I_{fc}(z) \quad (19)$$

where I_{mc} and I_{fc} are the light intensity on the catalyst coating of the monolith and the fiber respectively. R_f is the fiber radius; R_m is the average distance between the z -axis and the monolith.

2.5. Multi-physical model parameters

The variables and parameters in the photocatalytic CO₂ reduction system can be divided into seven categories, as shown in Table 1. The fundamental structure of the proposed model in this work is same as Wang's model [31], except the bigger reaction surface area from the additional transparent glass balls with photocatalyst coating. The flow channel near the balls gets narrowed, which obstruct the fluid flows. The geometric parameters are obtained from the specific size of the true OFMR. The hydrodynamic and mass transfer parameters are calculated by the aforementioned equations, and the radiation parameters are obtained by literature [27]. The CO₂ acts as the primary reactant while water vapor as the pivotal factor affecting the photoreaction rate. From the experiment data, the inlet concentrations of CO₂ and H₂O are estimated as 98% and 2%, that is, pure CO₂ with saturated water vapor [28].

2.6. Validation of numerical results

The proposed model of optical fiber monolith reactor with glass balls is developed

from the previous model without glass balls, which has been studied by Liou et al. [28], Lin and Valsaraj [26]. For the traditional optical fiber monolith reactor without glass balls, the effects of fiber position and operating parameters on the photocatalytic CO₂ reduction have been investigated by using CFD method in our previous work [29], which are in good agreements with the experimental data of Liou et al. [28]. It shows that the multi-physics modeling and computational methods are reliable enough to further study the optimized structure of the photoreactor with transparent glass balls in this work.

3. Results and discussion

The variations of product concentration, reaction rate and fluid velocity are presented to explain the photocatalytic CO₂ reduction characteristics in optical fiber monolith reactor with glass balls. The effects of the ball number and location, circle and layer numbers are discussed.

3.1. Variable fields

As an illustrative case, the proposed model with 15 glass balls coated with photocatalyst is analyzed, and the volume of each glass ball is 0.01 mm³.

The CH₃OH concentration and reaction rate along the *z*-axis in the proposed model are shown in Fig. 3. It can be seen that the methanol concentration increases along the *z*-axis while the reaction rate decreases clearly on the contrary. Because the reactants flow into the reactor from the inlet and then react accompanying with the flow, the reactant concentrations near the entrance are high and becomes lower in the process of flow, so the reaction rate decreases gradually along the flow channel.

Considering the symmetric structure of OFMR, the methanol concentration distributions in two models are shown in Fig. 4, where the product concentration increases clearly in the flow direction. Moreover, the concentration distribution of the proposed model is almost similar to that of the traditional one, while the average outlet CH₃OH concentration in the proposed model is higher due to the increased reaction surface from the balls coated with photocatalyst. For better displaying the changing trends, Fig. 5 shows the average CH₃OH concentration along the z-axis in the traditional and proposed models. When z equals 5 mm, the average concentration of CH₃OH for the proposed model is 9.707e-6 mol/m³, increases by 1.02% compared with the traditional model with the CH₃OH concentration of 9.6081e-6 mol/m³. While at the outlet, the CH₃OH concentration increases by 0.8%. Due to the reduced reaction rate along the z-axis, the methanol concentration increases slowly and arrives at the maximum at the outlet of the photoreactor. As seen from the results, it is feasible to promote the CH₃OH yield by adding the transparent balls coated with photocatalysts into the OFMR. However, the increase of the CH₃OH yield is still of limited, so the emphases are place upon the photoreactor structure improvement by adding transparent balls in the following research.

The fluid velocity in the photoreactor is shown in Fig. 6. It can be observed that the velocities near the fiber, monolith and balls are small due to the near-wall effect. Compared with the traditional model without balls shown in Fig. 6(a), the maximum local velocity becomes bigger and the minimum local velocity is smaller at the ball center plane where the flow channel gets narrow due to the disturbance of the glass

balls to some extent, as shown in Fig. 6(b).

3.2. Effects of ball number

Based on the fixed volume of each ball, the effects of ball number on the photocatalytic CO₂ reduction are investigated. For the traditional model, the calculated outlet methanol concentration is 1.2664e-5 mol/m³. Keeping other parameters same as the traditional model, the proposed model with different ball numbers at one layer and one circle, as shown in Fig. 7, is simulated. During the simulation, the balls with the same axial coordinate, z_{gs} , distribute uniformly around the fiber. Moreover, the effect of z_{gs} is also studied. The outlet average methanol concentrations at different ball numbers and axial coordinate z_{gs} are shown in Fig. 8. It can be observed that the outlet methanol concentration increases with increasing the ball number, because the balls coated with photocatalyst lead to the increased reaction surface, thus a high product concentration. The outlet CH₃OH concentration rises firstly and decreases later as the z_{gs} increases. For the current geometric structure, the model with 15 balls at one layer and one circle is preferred when the r_{gs} equals 0.65 mm.

3.3. Effects of ball location

The influences of ball location on the outlet CH₃OH average concentration in different models are studied, where the ball location is defined by the radial coordinate and axial coordinate, r_{gs} and z_{gs} as shown in Fig. 2. Fig. 9 shows the outlet CH₃OH average concentrations at various z_{gs} and r_{gs} . When the z_{gs} is constant, the product concentration decreases clearly with the increase of r_{gs} . The smaller the r_{gs} is, the closer to the fiber the glass balls are and the more photons the photocatalysts coated on the

glass balls could receive. Therefore, the concentration of CH₃OH gets lower along with the r_{gs} . When the z_{gs} is bigger than 0.5mm, the changing trends of CH₃OH average concentration are similar, that is, it decreases with increasing the z_{gs} , as shown in Fig. 9(b). The reaction rate decreases as the axial coordinate (z value) increases, so when the balls are close to the inlet, the reaction rate is big and the yield of the products is relatively large. When the z_{gs} arrives at 3mm, the proposed photoreactor with balls fails in increasing the production, and the outlet CH₃OH concentration is even lower than the traditional model. However, when the balls are close to the inlet with z_{gs} equal to 0.2mm, 0.3mm, 0.4mm, the outlet CH₃OH concentrations differ widely from other cases. Although the reaction rate is bigger near the inlet, the disturbance of the balls in the flow-path results in an unfavorable effect on the photoreaction, as shown in Fig. 9(a). As a result, a relatively optimum methanol production of about $1.2764 \times 10^{-5} \text{ mol/m}^3$ is reached when the r_{gs} equals 0.69mm and z equals 0.4mm.

3.4. Effects of layer number

In the single-layer model as discussed above, the production decreases with increasing the axial distance, so the multi-layer balls set at the inlet are recommended. By increasing the ball layer along the axial direction, the photocatalytic CO₂ reduction in optical fiber monolith reactor is numerically investigated. Fig. 10 shows the proposed models with multi-layer balls, which can be regarded as a superposition of some single-layer balls at different axial locations. For the first layer closest to the inlet, the axial coordinate z_{gs} is set 0.2mm. Subsequently, the ball layer increases and the distance between two adjacent layers is 0.3mm. For each layer, a relatively optimum radial

location is set on account of previous calculation results shown in Fig. 9. When the axial coordinate of balls (z_{gs}) equals 0.2mm, the optimum radial location is 0.9mm. If z_{gs} is greater than 0.4mm, the relatively better radial location for the balls is the same, namely r_{gs} equals 0.65mm.

For the multi-layer balls, the outlet average methanol concentration is shown in Fig. 11. As the layer number n_l increases, the product yield first increases and then decreases. The optimal layer number is 8, at which the product concentration reaches the peak value of $1.2990\text{e-}5 \text{ mol/m}^3$. In general, as the ball layer increases, the surface area for photocatalytic CO_2 reduction will increase because the balls are coated with photocatalyst evenly. But the disturbance of the balls on the flow also becomes strong, and the promoting effect on the methanol formation gets weak when the balls are far away from the inlet. As a result, there must exist an optimum layer number for the model of multi-layer balls.

3.5. Effects of circle number

Besides the multi-layer configuration, increasing the ball circle is another method to improve photocatalytic CO_2 reduction in optical fiber monolith reactor. Based on one layer model, the model with multi-circle balls is developed. As aforementioned, more ball number in one circle is of benefit to the outlet methanol concentration. The multi-circle balls model can also be regarded as a superposition of the single-circle model. Due to the fixed ball volume and the limitation of channel space, only 3 circles are set in the flow-path, as shown in Fig. 12. The circle closest to the fiber is defined as circle a, the middle circle is circle b and the circle closest to the monolith is circle c. The

numbers of balls in circle a, b, c are 15, 20, 24 and the radial distances are 0.65mm, 0.93mm, 1.21mm, respectively.

The variation of outlet CH₃OH concentration with the axial location for multi-circle model is shown in Fig. 13. It can be seen that the CH₃OH production rises with increasing the circle number thanks to the increased reaction surface area from more circles of balls with photocatalyst films. For the fixed circle, the production decreases as the ball axial location increases, which is similar to the results of one layer and one circle model. As the aforementioned results, the reaction rate decreases with increasing the axial coordinate (z value), so when the balls are close to the inlet, the yield of the products is relatively big.

3.6. Multi-layer and multi-circle balls

For multi-layer and multi-circle model, the 2-circle and 3-circle multi-layer balls are studied. As an illustrative case, the model with 2-circle and 4-layer balls is schematically shown in Fig. 14, which is superposed by the single-layer balls with 2-circle along z -axis. The balls near the fiber are defined as circle a and the other circle near the monolith is circle b. The numbers of balls in circles a and b are 15 and 20, and the radial distances are 0.65mm and 0.93mm respectively. The axial distance to the inlet of the first layer is 0.2mm, and then the axial spaces of every adjacent two layers are all set as 0.3mm.

The outlet CH₃OH concentrations for the models with 2-circle and 3-circle multi-layer balls are shown in Fig. 15. It can be observed that the outlet CH₃OH average concentration increases with the layer number firstly and then decreases after 7 layers

for 2-circle model, and 5 layers for 3-circle model. Although more layer number increases the surface area for photoreaction, the disturbance of the balls to the flow also gets strong. The promoting effect on the methanol formation is weak when the balls are far away from the entrance. As a result, 7 layers and 5 layers are preferred for better photocatalytic CO₂ reduction in OFMR with 2-circle and 3-circle balls, as shown in Fig. 15. The CH₃OH concentrations for the 2-circle and 7-layer balls model, 3-circle and 5-layer balls model increases by 6.27% and 11.43% respectively, compared with the traditional OFMR without balls.

4. Conclusions

The photocatalytic carbon dioxide reduction in a novel optical fiber monolith reactor with transparent glass balls is proposed. For the model with single-circle and single-layer balls, the outlet methanol concentration increases with increasing the ball number. In general, the closer the distance from the balls to the fiber and the inlet is, the higher the methanol production is. The methanol concentration rises with increasing the circle and layer numbers. The methanol concentrations for the 2-circle and 7-layer balls model, 3-circle and 5-layer balls model increases by 6.27% and 11.43% respectively, compared with the traditional optical fiber monolith reactor without glass balls, so the 3-circle and 5-layer configuration is recommended.

The photocatalytic reduction performance of carbon dioxide is improved for the proposed optical fiber monolith reactor, which indicates a new direction to the development and innovation of carbon dioxide photo-hydrogenation. In future studies, new types of carbon dioxide photoreactor with various geometric structures will emerge

in large numbers, which can effectively restrain greenhouse gas emission and mitigate energy shortage.

Acknowledgments

The financial supports for this research, from the National Natural Science Foundation of China (Grant No. 51776067) and the National Basic Research Program of China (Grant No. 2015CB251503), are gratefully acknowledged. The authors also thank the support provided by the Royal Society International Project of UK (IE150489).

Reference

- [1] Tahir M, Amin NS. Advances in visible light responsive titanium oxide-based photocatalysts for CO₂ conversion to hydrocarbon fuels. *Energy Convers Manag* 2013;76:194–214.
- [2] Yang MQ, Xu YJ. Photocatalytic conversion of CO₂ over graphene-based composites: current status and future perspective. *Nanoscale Horizons* 2016;1:185–200.
- [3] Delavari S, Amin NS. Photocatalytic conversion of CO₂ and CH₄ over immobilized titania nanoparticles coated on mesh: Optimization and kinetic study. *Appl Energ* 2016;162:1171–85.
- [4] Wan KKW, Li DHW, Pan W, Lam JC. Impact of climate change on building energy use in different climate zones and mitigation and adaptation implications. *Appl Energ* 2012;97(3):274–82.
- [5] Lo CC, Hung CH, Yuan CS, Wu JF. Photoreduction of carbon dioxide with H₂ and H₂O over TiO₂ and ZrO₂ in a circulated photocatalytic reactor. *Sol Energy Mater Sol Cells* 2007;91:1765–74.
- [6] Kočí K, Matějová L, Kozák O, Čapek L, Valeš V, Reli M, et al. ZnS/MMT nanocomposites: The effect of ZnS loading in MMT on the photocatalytic reduction of carbon dioxide. *Appl Catal B Environ* 2014;158–159:410–7.
- [7] Castellani B, Gambelli AM, Morini E, et al. Experimental Investigation on CO₂ Methanation Process for Solar Energy Storage Compared to CO₂-Based Methanol Synthesis. *Energies* 2017;10(7):855.

- [8] Macdowell N, Florin N, Buchard A, et al. An overview of CO₂ capture technologies. *Energy Environ Sci* 2010; 3(11):1645–69.
- [9] Chu F, Liu Y, Yang L, Du X, Yang Y. Ammonia escape mass transfer and heat transfer characteristics of CO₂ absorption in packed absorbing column. *Appl Energ* 2017;205:1596–604.
- [10] Chu F, Yang L, Du X, Yang Y. CO₂ capture using MEA (monoethanolamine) aqueous solution in coal-fired power plants: Modeling and optimization of the absorbing columns. *Energy* 2016;109:495–505.
- [11] Chu F, Yang L, Du X, Yang Y. Mass transfer and energy consumption for CO₂ absorption by ammonia solution in bubble column. *Appl Energ* 2017;190:1068–80.
- [12] Castellani B, Morini E, Bonamente E, et al. Experimental investigation and energy considerations on hydrate-based biogas upgrading with CO₂ valorization. *Biomass & Bioenergy* 2017;105:364–72.
- [13] Ola O, Maroto-Valer MM. CO₂ Conversion into Valuable Fuels Using Chromium Based Supports. *Energy Procedia* 2014;63:7963–7.
- [14] Wee JH. A review on carbon dioxide capture and storage technology using coal fly ash. *Appl Energ* 2013;106(11):143–51.
- [15] Ramachandriya KD, Kundiyana DK, Wilkins MR, et al. Carbon dioxide conversion to fuels and chemicals using a hybrid green process. *Appl Energ* 2013; 112(4):289–99.
- [16] Pérez-Fortes M, Schöneberger JC, Boulamanti A, et al. Methanol synthesis using

- captured CO₂, as raw material: Techno-economic and environmental assessment. *Appl Energ* 2016;161:718–32.
- [17] Reilly K, Wilkinson DP, Taghipour F. Photocatalytic water splitting in a fluidized bed system: Computational modeling and experimental studies. *Appl Energ* 2018; 222:423–36.
- [18] Ola O, Maroto-Valer MM. Review of material design and reactor engineering on TiO₂ photocatalysis for CO₂ reduction. *J Photochem Photobiol C Photochem Rev* 2015;24:16–42.
- [19] Puangpetch T, Chavadej S, Sreethawong T. Hydrogen production over Au-loaded mesoporous-assembled SrTiO₃ nanocrystal photocatalyst: Effects of molecular structure and chemical properties of hole scavengers. *Energy Convers Manag* 2011;52:2256–61.
- [20] Yuan K, Yang L, Du X, Yang Y. Performance analysis of photocatalytic CO₂ reduction in optical fiber monolith reactor with multiple inverse lights. *Energy Convers Manag* 2014;81:98–105.
- [21] Chu F, Li S, Chen H, Yang L, Ola O, Maroto-Valer M, et al. Modeling photocatalytic conversion of carbon dioxide in bubbling twin reactor. *Energy Convers Manag* 2017;149:514–25.
- [22] Cheng YH, Nguyen VH, Chan HY, Wu JCS, Wang WH. Photo-enhanced hydrogenation of CO₂ to mimic photosynthesis by CO co-feed in a novel twin reactor. *Appl Energ* 2015;147:318–24.
- [23] Wu JCS, Wu TH, Chu T, Huang H, Tsai D. Application of Optical-fiber

- Photoreactor for CO₂ Photocatalytic Reduction. *Top Catal* 2008;47:131–6.
- [24] Tahir M, Amin NS. Recycling of carbon dioxide to renewable fuels by photocatalysis: Prospects and challenges. *Renew Sustain Energy Rev* 2013;25:560–79.
- [25] Xiong Z, Lei Z, Ma S, Chen X, Gong B, Zhao Y, et al. Photocatalytic CO₂ reduction over V and W codoped TiO₂ catalyst in an internal-illuminated honeycomb photoreactor under simulated sunlight irradiation. *Appl Catal B Environ* 2017;219:412–24.
- [26] Lin H, Valsaraj KT. An optical fiber monolith reactor for photocatalytic wastewater treatment. *AIChE J* 2006;52:2271–80.
- [27] Wu JCS, Lin HM, Lai CL. Photo reduction of CO₂ to methanol using optical-fiber photoreactor. *Appl Catal A Gen* 2005;296:194–200.
- [28] Liou PY, Chen SC, Wu JCS, Liu D, Mackintosh S, Maroto-Valer M, et al. Photocatalytic CO₂ reduction using an internally illuminated monolith photoreactor. *Energy Environ Sci* 2011;4:1487–94.
- [29] Wang T, Yang L, Du X, Yang Y. Numerical investigation on CO₂ photocatalytic reduction in optical fiber monolith reactor. *Energy Convers Manag* 2013;65:299–307.
- [30] Boyjoo Y, Ang M, Pareek V. Light intensity distribution in multi-lamp photocatalytic reactors. *Chem Eng Sci* 2013;93:11–21.
- [31] Wang ZY, Chou HC, Wu JCS, Tsai DP, Mul G. CO₂ photoreduction using NiO/InTaO₄ in optical-fiber reactor for renewable energy. *Appl Catal A Gen*

- 2010;380:172–7.
- [32] Rathore MM, Kapuno R. Engineering Heat Transfer, Second Edition[M]. Jones and Bartlett Publishers, Inc. 2010.
- [33] Tahir M, Amin NS. Photocatalytic CO₂ reduction and kinetic study over In/TiO₂ nanoparticles supported microchannel monolith photoreactor. Appl Catal A Gen 2013;467:483–96.
- [34] Denny F, Scott J, Peng GD, Amal R. Channelled optical fibre photoreactor for improved air quality control. Chem Eng Sci 2010;65:882–9.
- [35] Harriott P. Chemical reactor design. Marcel Dekker; 2003.
- [36] Marinangeli RE, Ollis DF. Photoassisted heterogeneous catalysis with optical fibers: I. Isolated single fiber. AIChE J 1977;23:415–26.
- [37] Peill NJ, Hoffmann MR. Development and Optimization of a TiO₂-Coated Fiber-Optic Cable Reactor: Photocatalytic Degradation of 4-Chlorophenol. Environ Sci Technol 1995; 29(12):2974.
- [38] Choi W, Ko JY, Park H, Chung JS. Investigation on TiO₂-coated optical fibers for gas-phase photocatalytic oxidation of acetone. Appl Catal B Environ 2001;31:209–20.
- [39] Puma GL, Yue PL. A laminar falling film slurry photocatalytic reactor. Part I—model development. Chem Eng Sci 1998;53:2993–3006.

Graphical abstract

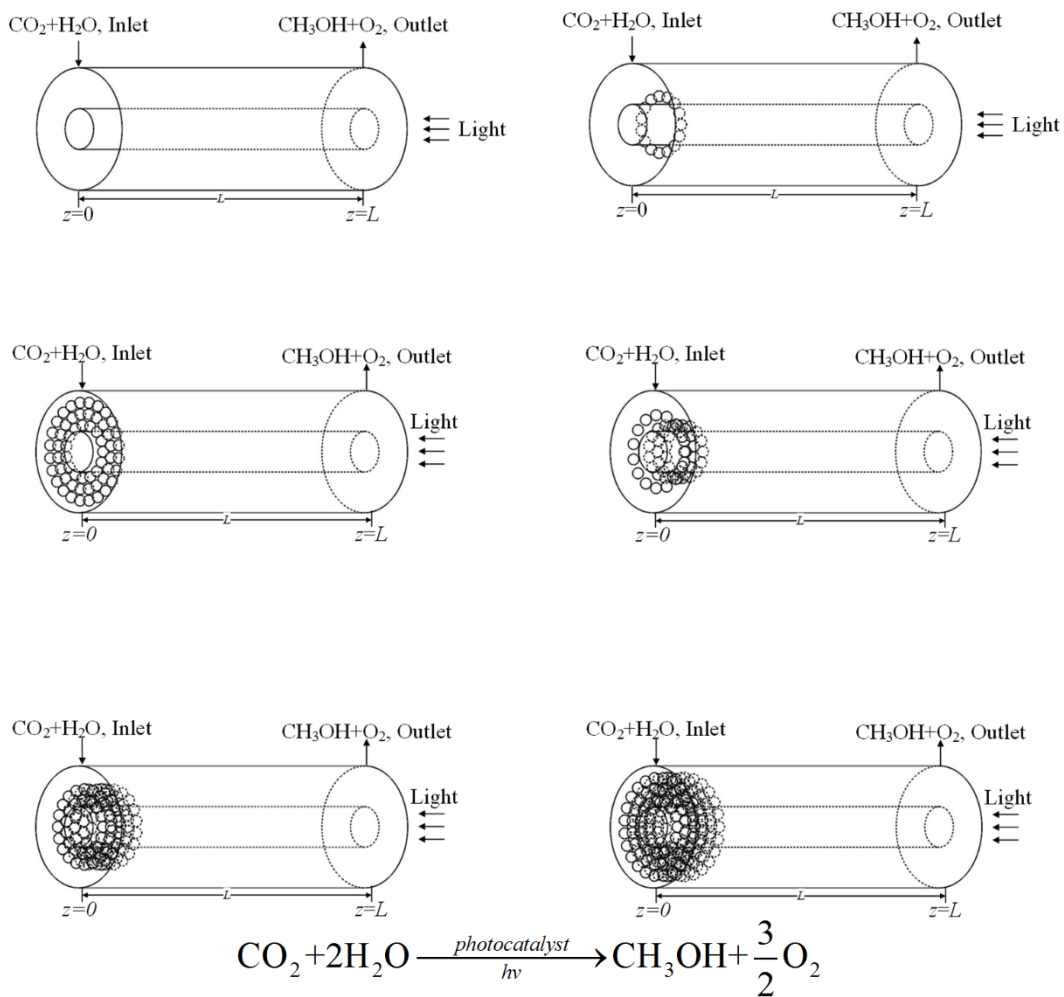


Table 1

The parameters of the proposed model.

Type	Variables	Values	Unit
Geometry	d_f	1	mm
	R_m	1.5	mm
	R_f	0.5	mm
	V_{gs}	0.01	mm ³
	D_{gs}	0.2673	mm
	R_{gs}	0.13365	mm
	L	10	mm
Fluid dynamics	δ	400	nm
	V_{inlet}	0.03	mm s ⁻¹
Mass transfer	D_{H_2O}	1.7327E-7	m ² s ⁻¹
	D_{CH_3OH}	1.31E-7	m ² s ⁻¹
	D_{O_2}	1.31E-7	m ² s ⁻¹
Radiation field	α	0.386	cm ⁻¹
	f_θ	0.762	Dimensionless
	β	1.95	cm ⁻¹
	ε	0.00102	nm ⁻¹
Kinetics	k_T	1.17E-10	m ⁴ s ⁻¹ mol ⁻²
UV input	I_{input}	424.6	W m ⁻²
Inlet concentration	C_{i,CO_2}	43.75	mol m ⁻³

C_{i,H_2O}

0.89

mol m⁻³

Fig. 1. Schematics of traditional and proposed OFMRs for one single channel. (a) Traditional, (b) proposed.

Fig. 2. Geometric structure of the proposed model.

Fig. 3. Methanol concentration and reaction rate in the photoreactor with 15 balls.

Fig. 4. Methanol concentration distribution in the photoreactor (unit in mol/m³). (a) Traditional model, (b) proposed model.

Fig. 5. Average methanol concentrations along z -axis in traditional model and proposed model with 15 balls.

Fig. 6. Fluid velocity distribution in the photoreactor (unit in m/s). (a) Traditional, (b) proposed.

Fig. 7. Schematics of the photoreactors with different ball numbers.

Fig. 8. Outlet average methanol concentration at different ball numbers and axial coordinates z_{gs} .

Fig. 9. Outlet average methanol concentration at various z_{gs} and r_{gs} .

Fig. 10. Schematics of the multi-layer balls model.

Fig. 11. Outlet methanol average concentration for multi-layer balls model.

Fig. 12. Schematics of the multi-circle balls model.

Fig. 13. Methanol concentration for multi-circle balls model.

Fig. 14. Schematics of the 2-circle and 4-layer balls model.

Fig. 15. Outlet methanol concentration for 2-circle and 3-circle multi-layer balls model.

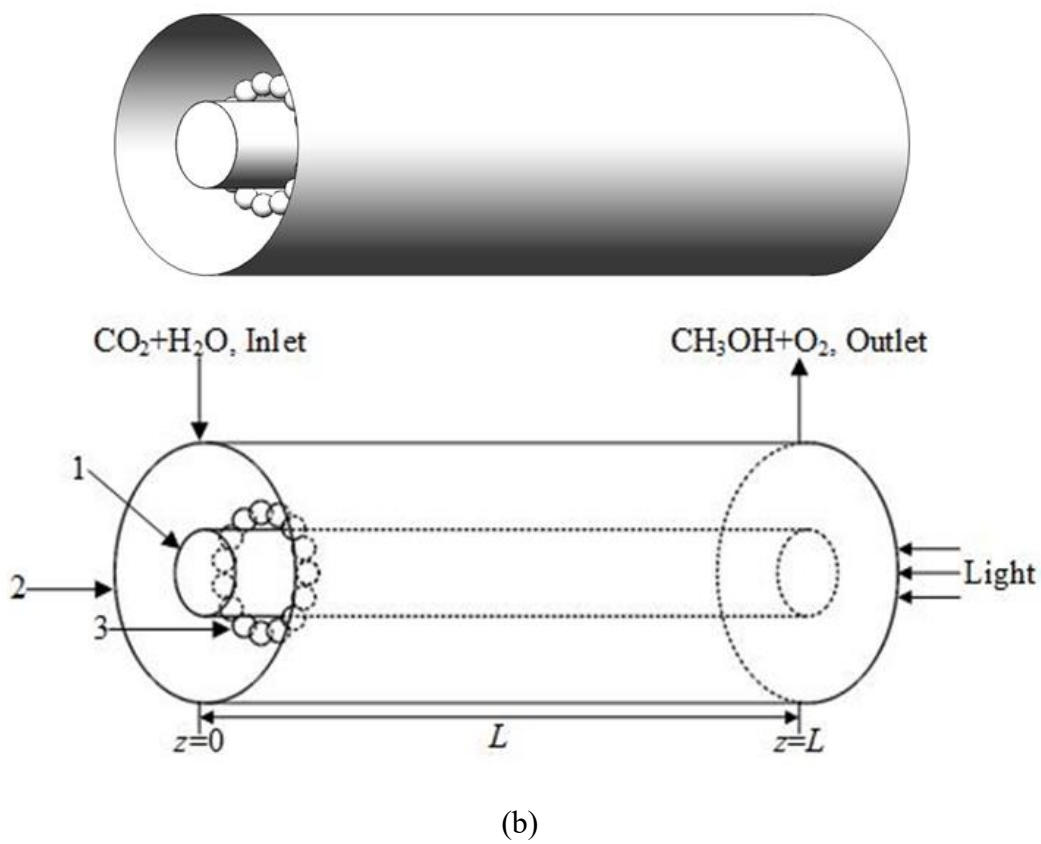
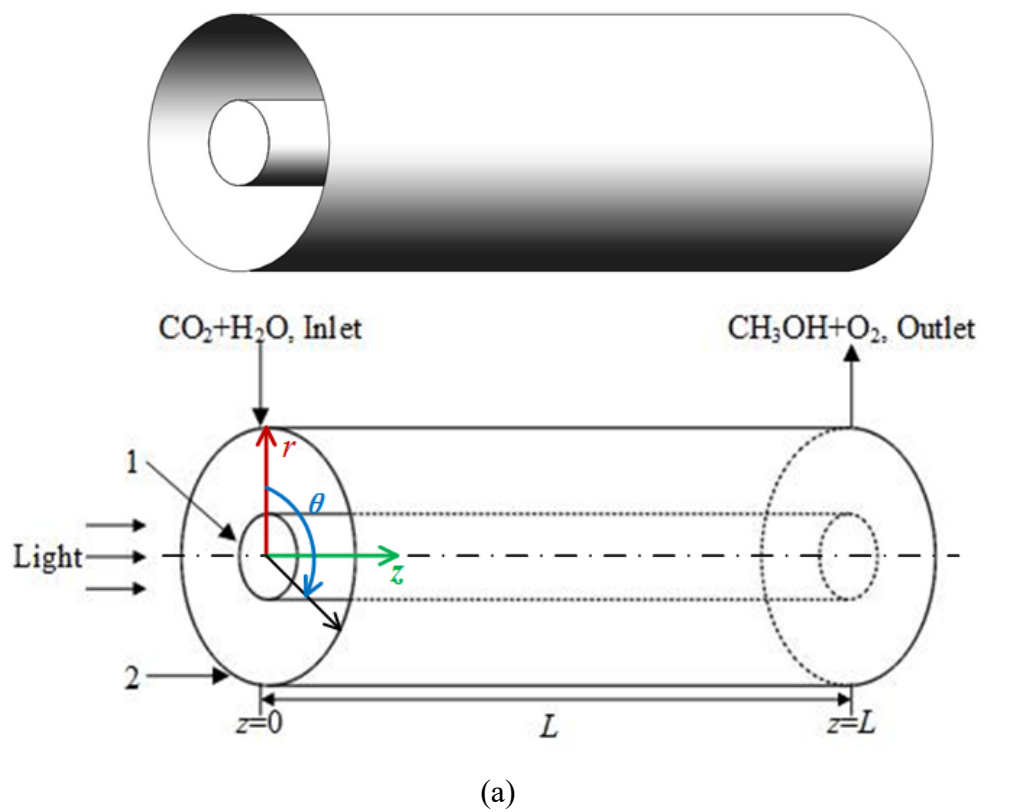


Fig. 1.

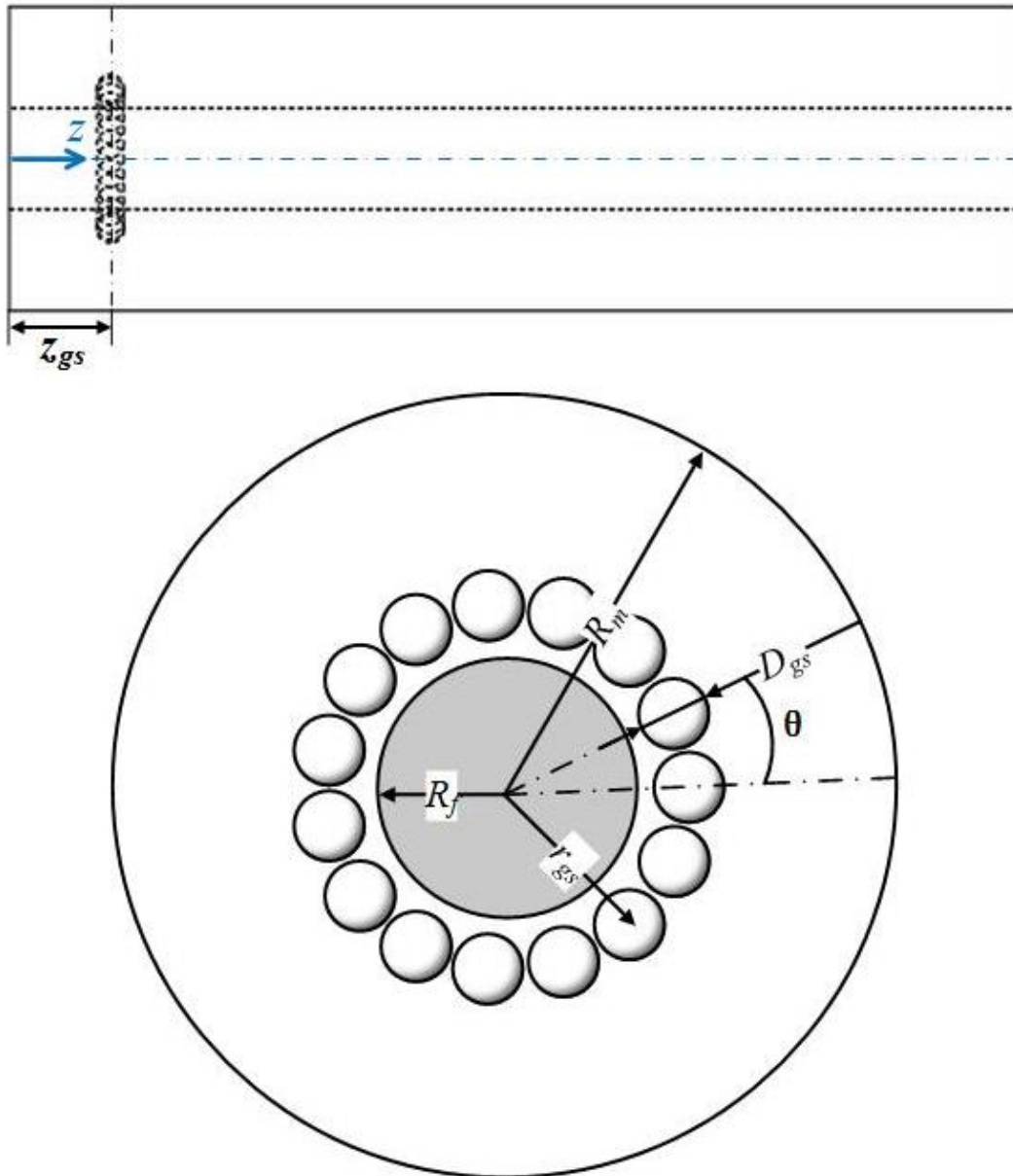


Fig. 2.

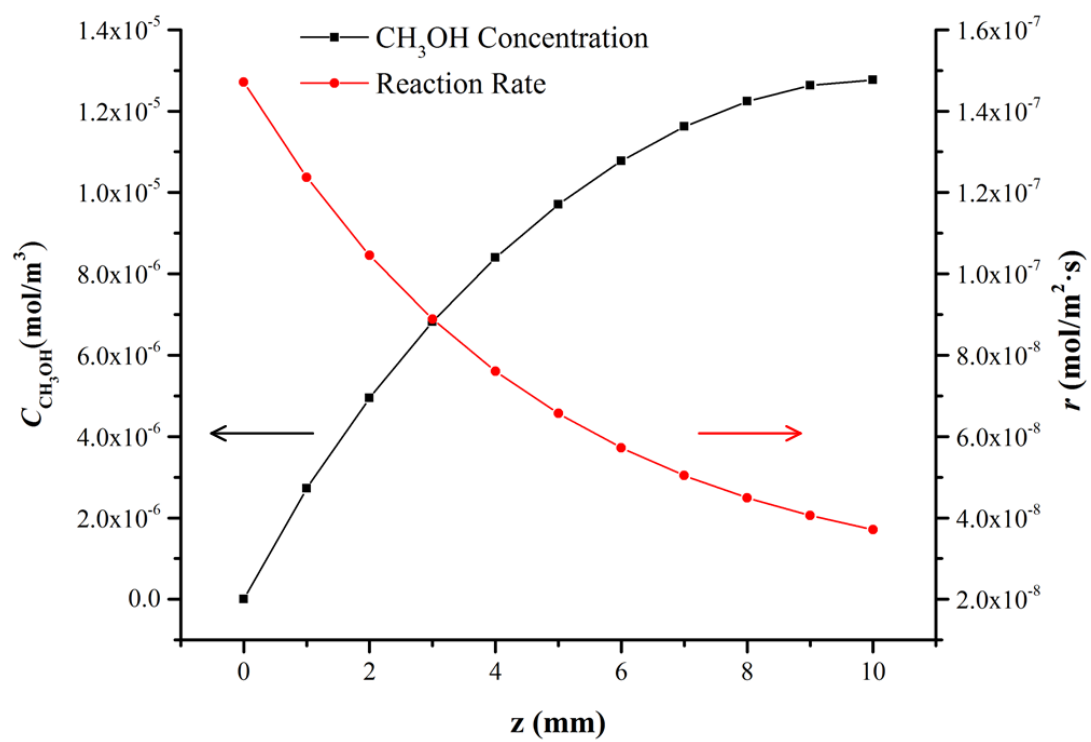
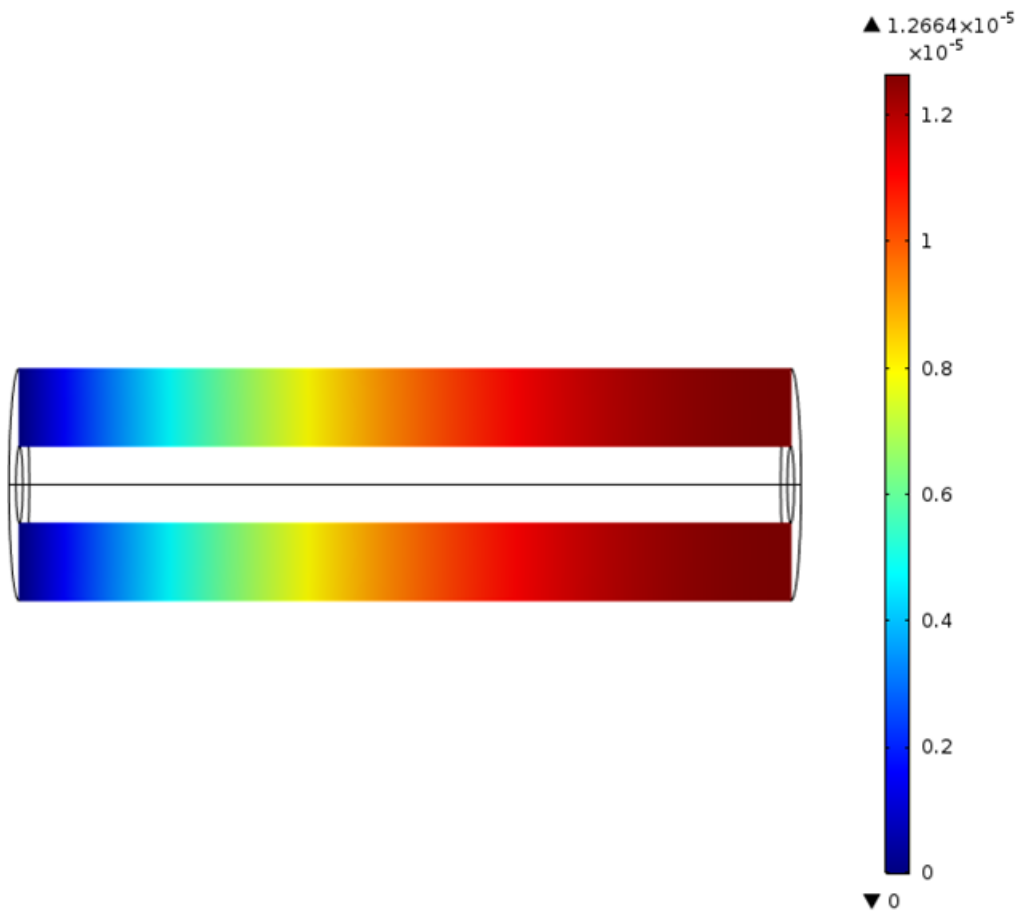
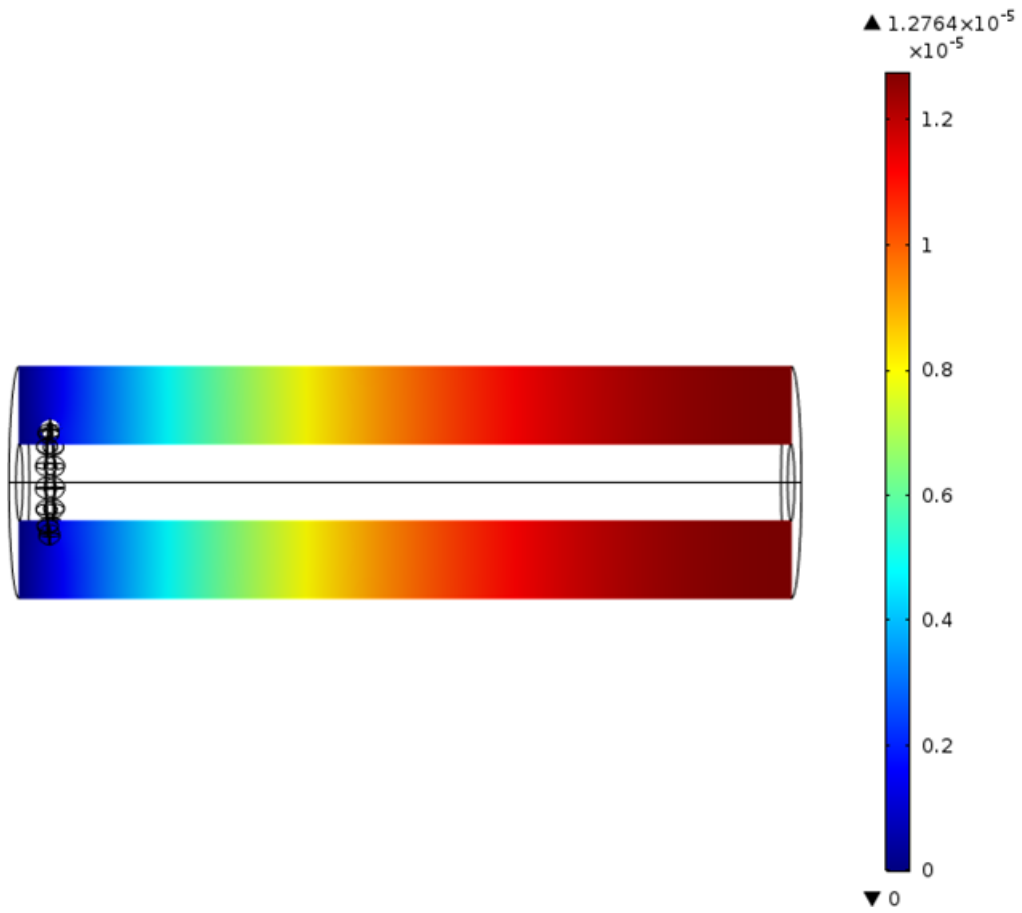


Fig. 3.



(a)



(b)

Fig. 4.

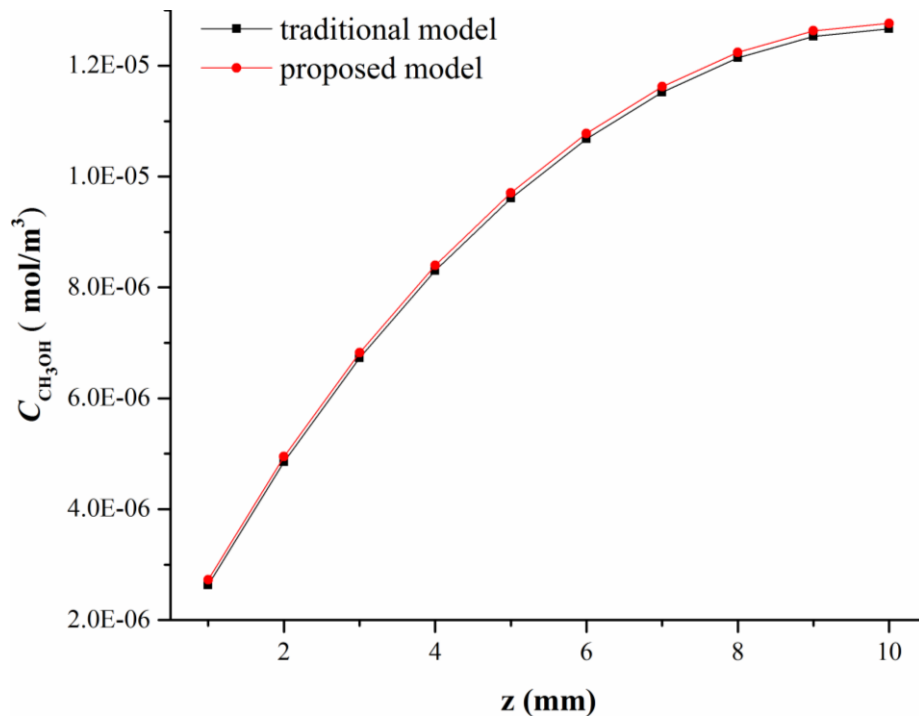
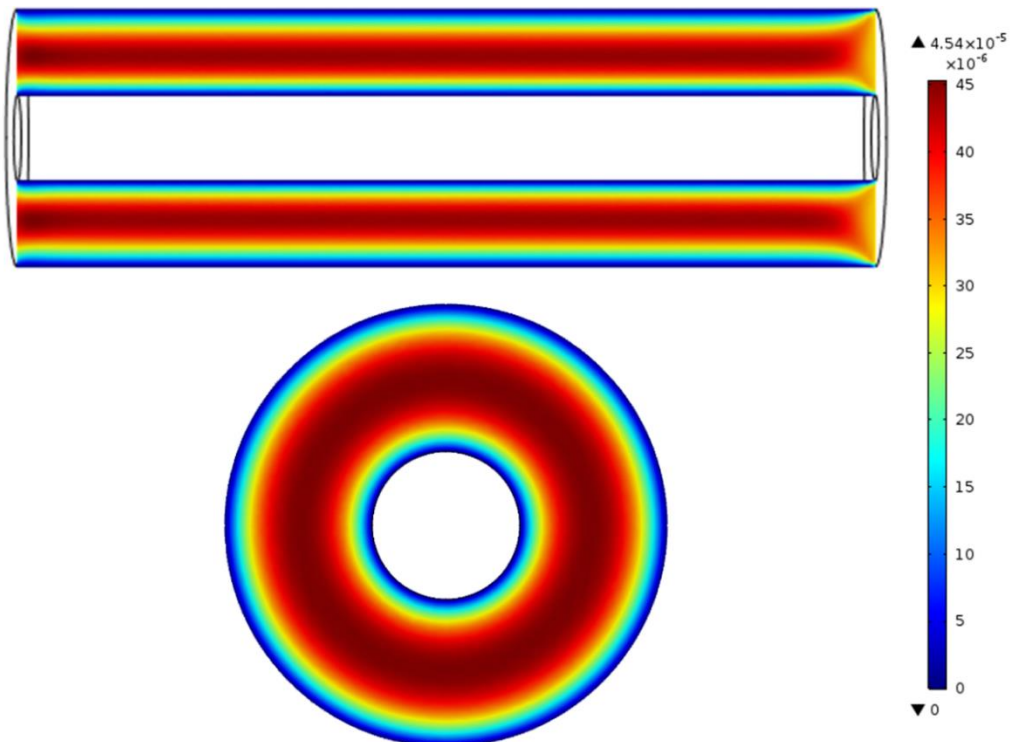
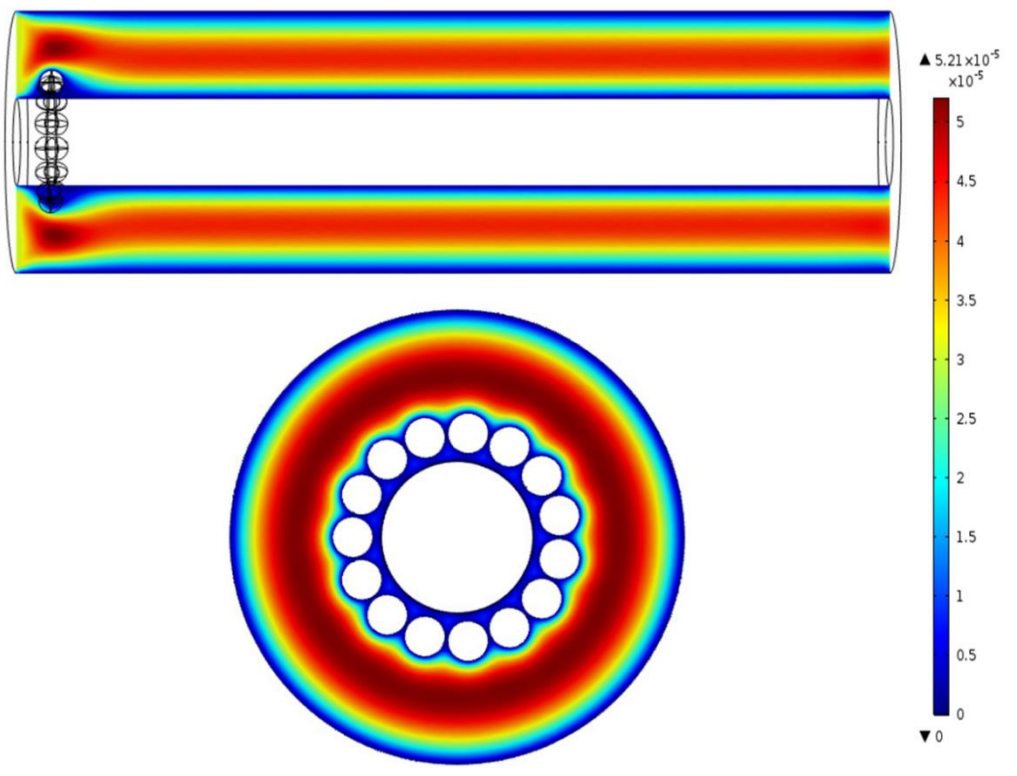


Fig. 5.



(a)



(b)

Fig. 6.

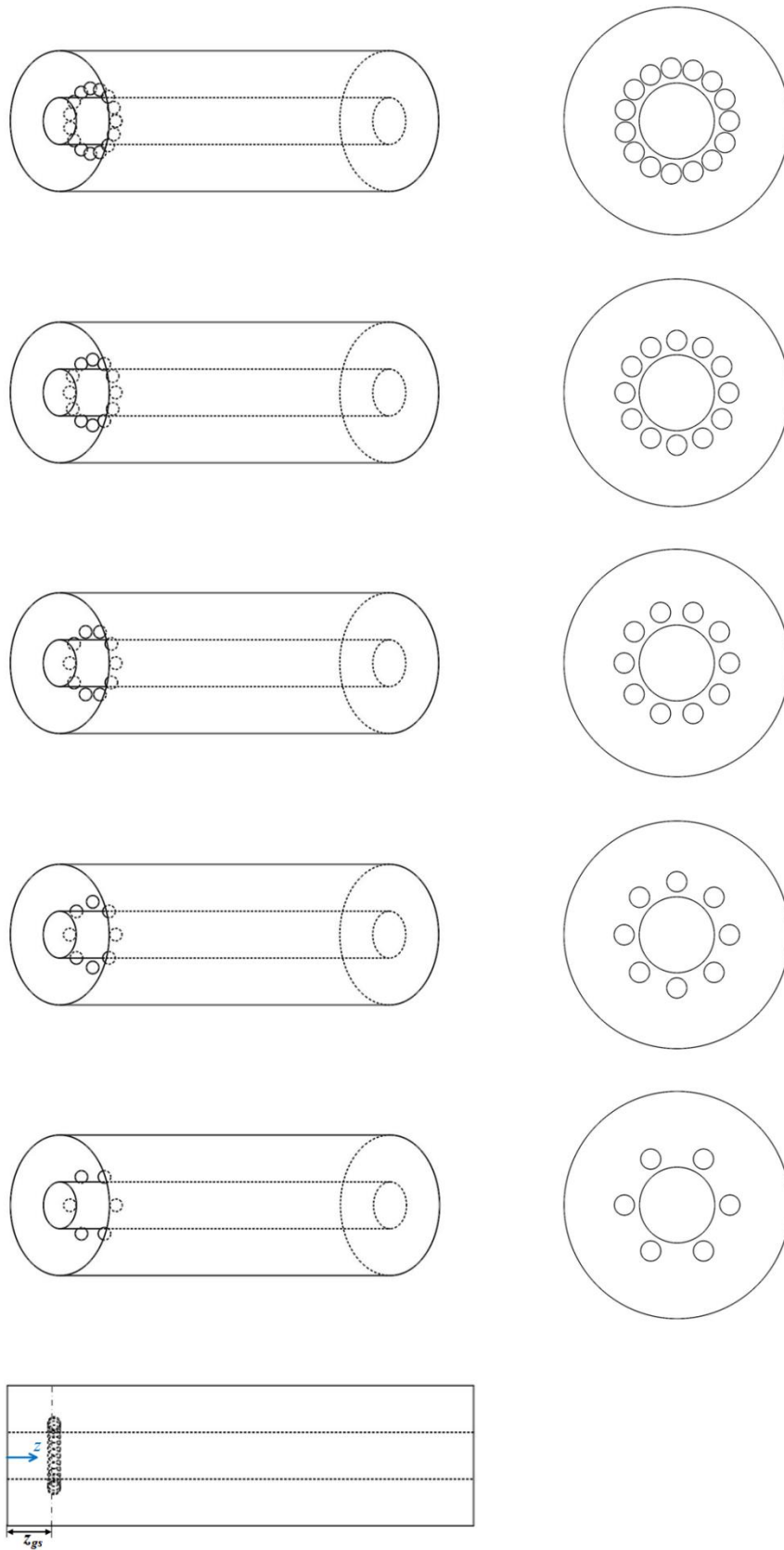


Fig. 7.

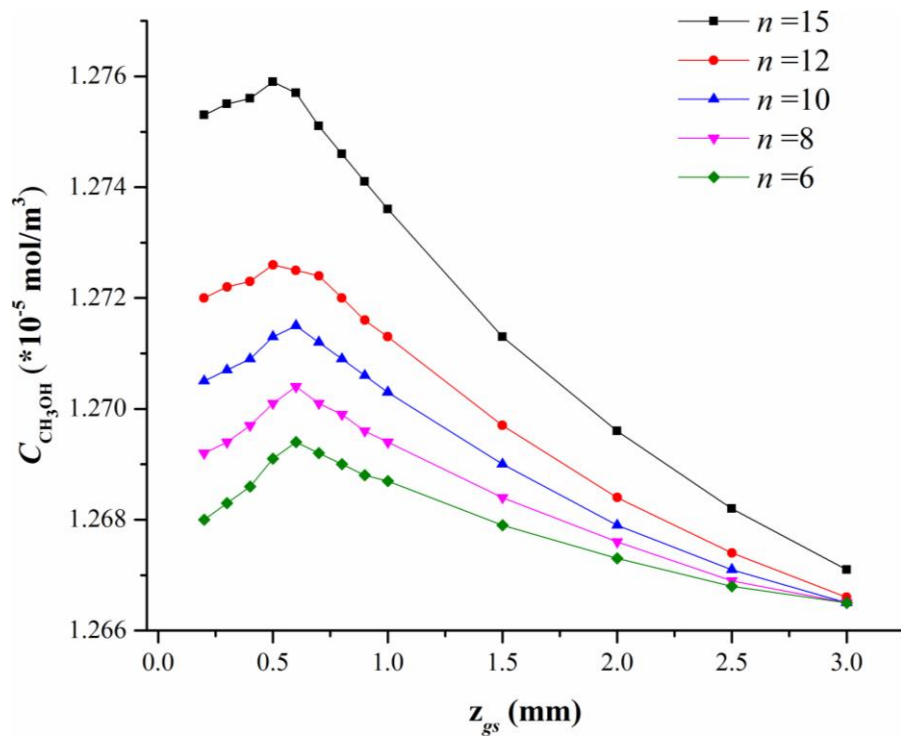
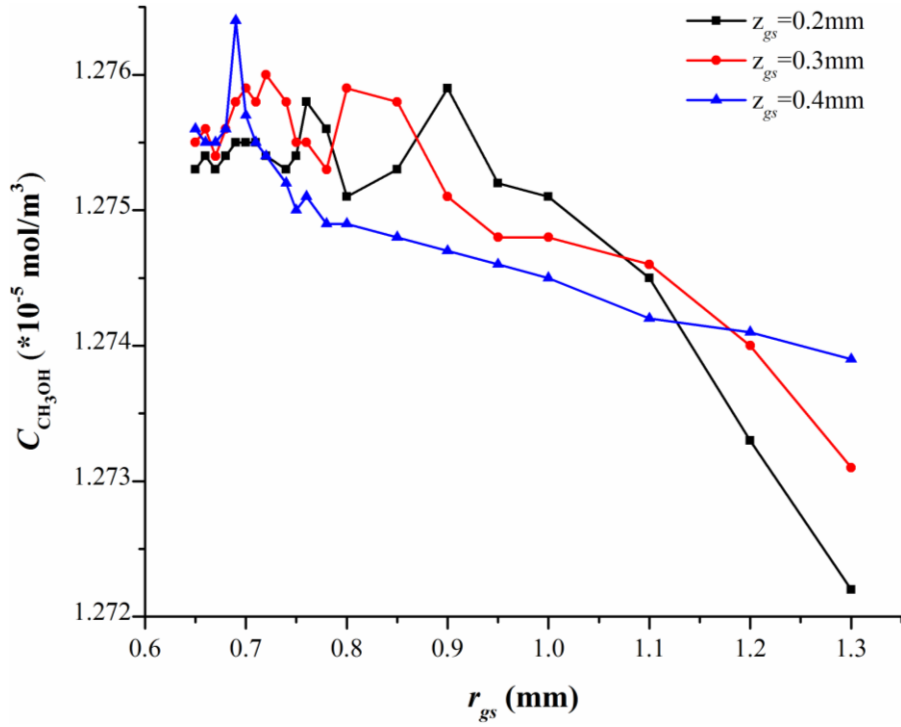
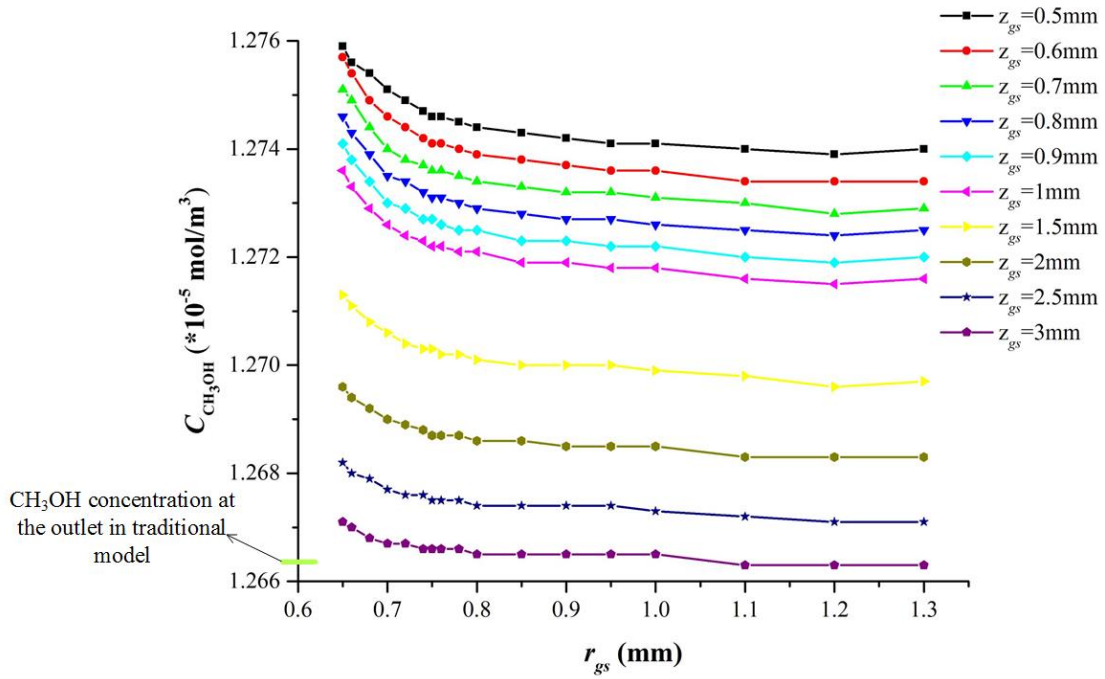


Fig. 8.



(a)



(b)

Fig. 9.

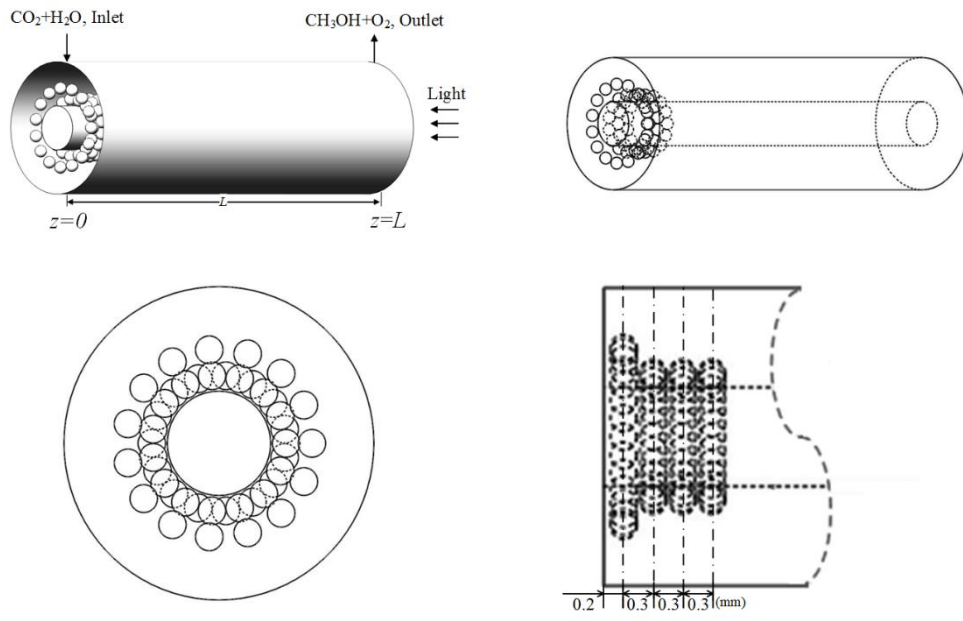


Fig. 10.

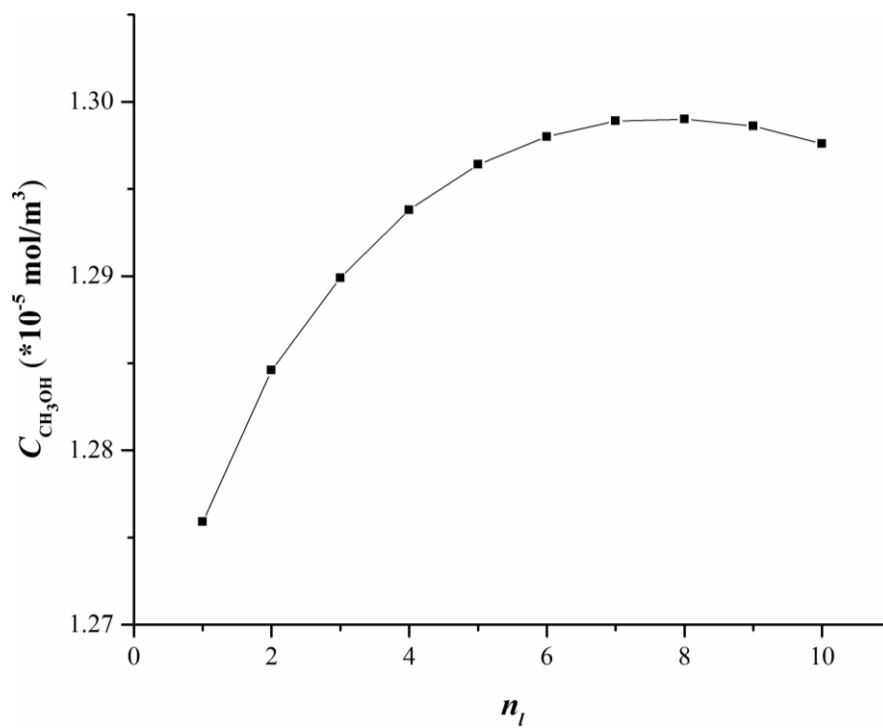


Fig. 11.

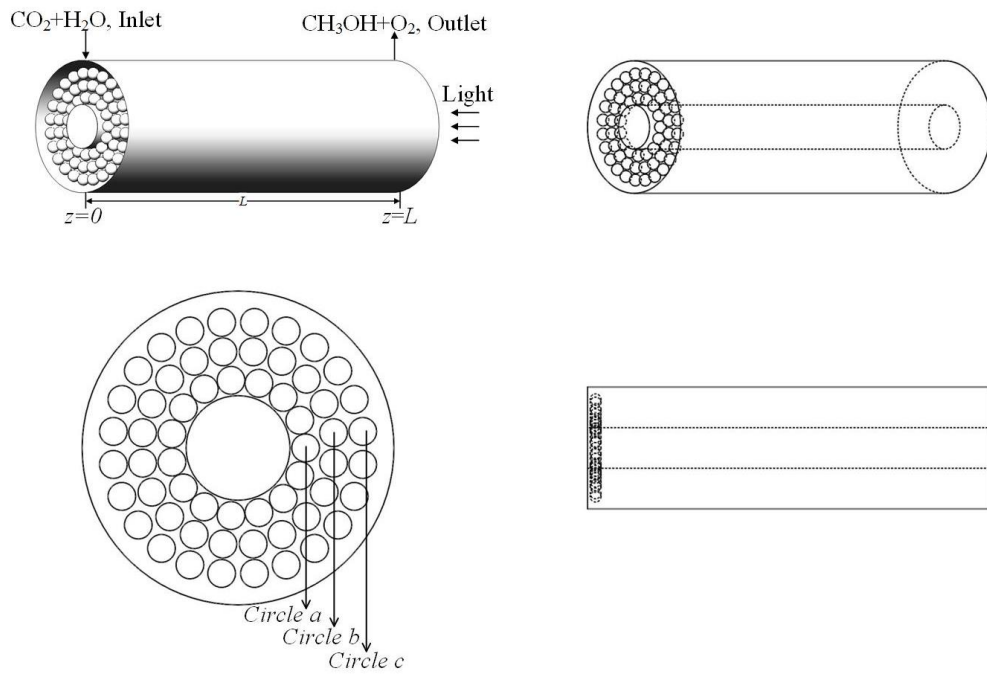


Fig. 12.

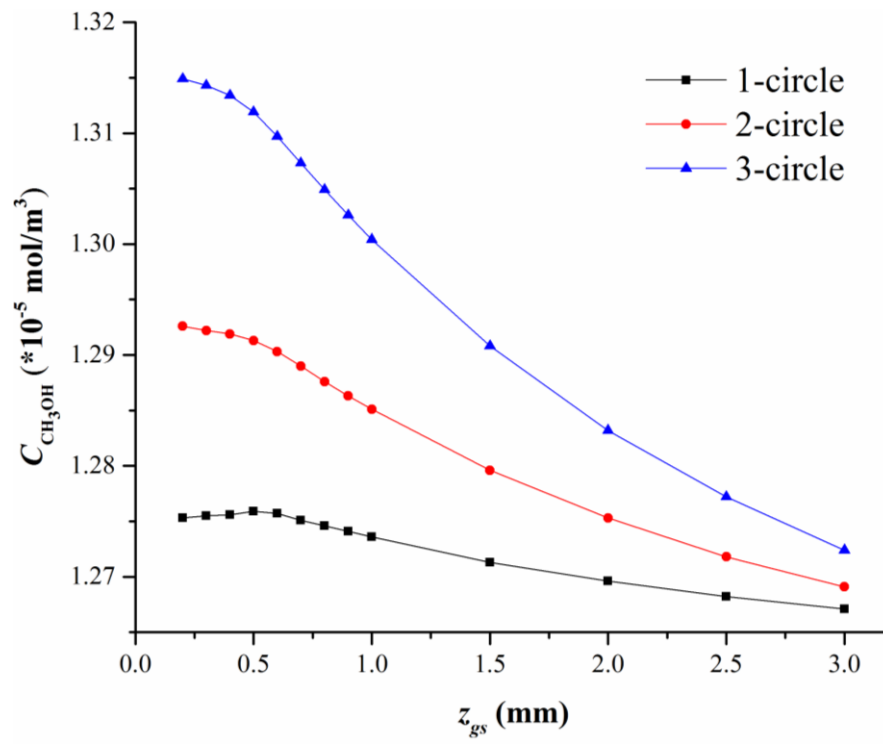


Fig. 13.

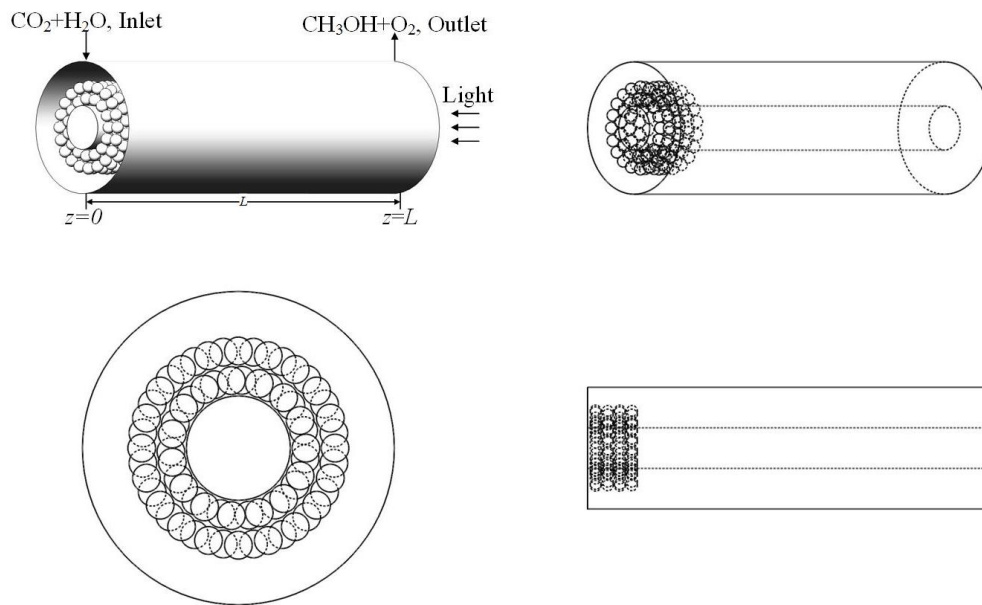


Fig. 14.

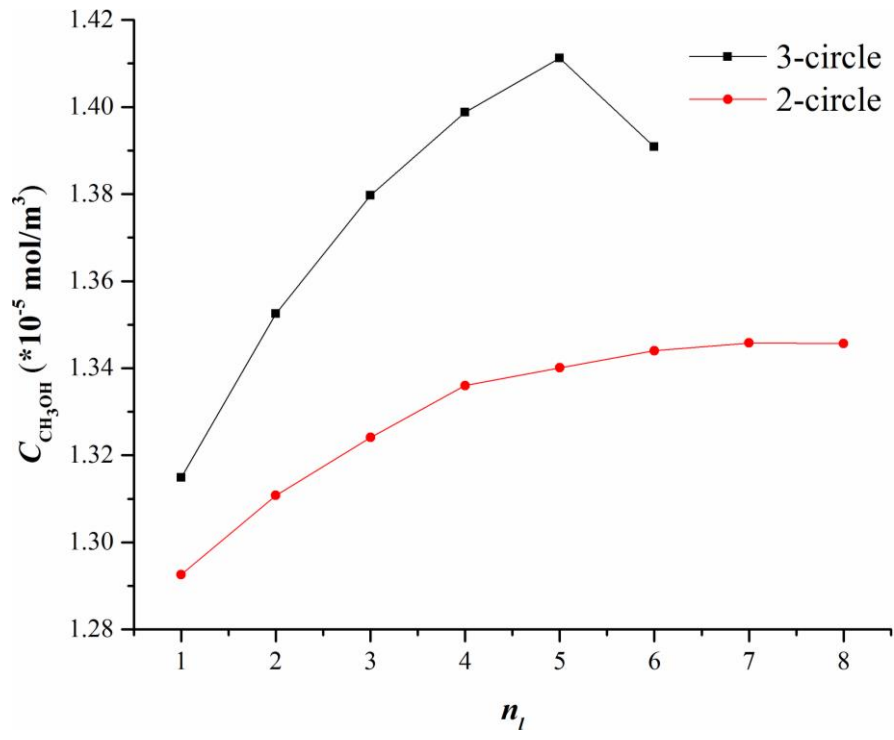


Fig. 15.